Materials Advances

ROYAL SOCIETY OF CHEMISTRY

PAPER

View Article Online
View Journal | View Issue

Cite this: *Mater. Adv.*, 2023, 4, 1363

Constructing amorphous/amorphous heterointerfaces in nickel borate/boride composites for efficient electrocatalytic methanol oxidation†

Ping Chen, Sai Zhang, Yu Fan, Wenlong Yang * and Xiliang Luo *

Owing to the inherently torpid kinetics involving an intricate multi-electron redox process, the methanol oxidation reaction (MOR) severely restrains the efficiency of direct methanol fuel cells (DMFCs). Herein, we put forward a room-temperature liquid-phase reaction strategy to construct an amorphous/amorphous heterojunction structure in a nickel borate/boride composite. It is found that the two sides of the heterointerface are composed of amorphous nickel boride (a-Ni_xB) nanoparticles and amorphous nickel borate (a-Ni-B_i) ultrathin nanosheets. Experimental measurements reveal that the amorphous/amorphous heterostructure endows the catalyst with enhanced charge transport capacity and stepped-up formation of electroactive NiOOH species, both of which contribute considerably to optimizing the catalytic kinetics for the MOR. As a result of the highly exposed active area and better intrinsic reactivity of catalytic sites, the amorphous Ni-B_i/Ni_xB (a-Ni-B_i/Ni_xB) hybrid catalyst exhibits outstanding electrocatalytic MOR activity with a low onset potential of 0.38 V *vs.* Ag/AgCl and a large current density of 213 mA cm^{-2} at a potential of 0.6 V *vs.* Ag/AgCl, which can be comparable to the best MOR performance of highly active Ni-based catalysts to date. This work opens new opportunities to design and synthesize efficient MOR electrocatalysts.

Received 16th November 2022,
Accepted 31st January 2023

DOI: 10.1039/d2ma01037b

rsc.li/materials-advances

Introduction

Direct methanol fuel cells (DMFCs) have emerged as a clean and renewable energy conversion technology that can directly accomplish electrical output by converting chemical energy, and they hold great promise to address the growing energy demand and environmental problem.[1–3] Nevertheless, a DMFC's overall conversion efficiency is frustratingly impeded by the kinetically slow methanol oxidation reaction (MOR) correlative to its complicated multi-electron transfer pathway, together with disadvantageous routes for the evolution of detrimental intermediates.[4,5] To date, despite the fact that a series of noble metals such as Pt- and Pd-based materials have been broadly recognized as the most effective MOR electrocatalysts to promote the sluggish methanol oxidation process, their extreme scarcity and daunting expensiveness as well as easy poisoning unfortunately render the realization of their large-scale utilization impractical for future commercialization.[6,7] In such regard, numerous research attempts have been unhesitatingly made to achieve affordable transition-metal-based catalysts on account of their desirable advantages of abundant reserves, low cost, ease of availability and reliable electrochemical properties.[8–11] Even so, limited by their slow charge transfer, deficient active sites and poor intrinsic catalytic activity, the electrocatalytic MOR performance of these materials is still far behind what we expect and needs significant promotion so as to catch up with the requirement of the commercial application of DMFCs.[12–14]

As reported recently, heterointerface engineering, especially for constructing heterostructures based on ultrathin two-dimensional (2D) nanomaterials, has attracted considerable attention in the electrochemical field owing to the impressive synergetic effects between ultrathin 2D structures and atomic-level coupled interactions of different components on electrocatalysis, which can not only allow for more exposed heterojunctions as catalytically active centres on the surface of catalysts, but also appreciably modulate the surface charge distribution for optimizing the reaction kinetics, as a consequence, dramatically improving the catalytic performance of electrocatalysts.[15–20] To date, relevant research studies have mainly concentrated on crystalline/crystalline heterostructures

Key Laboratory of Optic-electric Sensing and Analytical Chemistry for Life Science, MOE, Key Laboratory of Analytical Chemistry for Life Science in Universities of Shandong, College of Chemistry and Molecular Engineering, Qingdao University of Science and Technology, Qingdao 266042, P. R. China.
E-mail: wlyang@qust.edu.cn, xiliangluo@qust.edu.cn

† Electronic supplementary information (ESI) available. See DOI: https://doi.org/10.1039/d2ma01037b

by virtue of their well-defined heterointerfaces along with available synthetic strategies and structural characterization methods. Nowadays, increasing efforts have been intensely devoted to pursuing amorphous/crystalline heterostructures since amorphous electrocatalysts usually exhibit remarkable superiority to their crystalline counterparts in facilitating the electrocatalytic process.[21–24] Therefore, it can be deliberately anticipated that the amorphous/amorphous heterojunction confined in ultrathin 2D structures will increase drastically both the number and intrinsic reactivity of active sites, enabling the realization of highly active electrocatalysts for the MOR. However, to the best of our knowledge, the construction of amorphous/amorphous heterostructures in ultrathin 2D nanosheets has rarely been reported to date, which is mainly due to the following aspects: (1) the isotropic nature of amorphous materials certainly makes the formation of nanostructures with ultrathin 2D configuration challenging (the growth mechanism of which relies principally on the inherent directionality of lattices). (2) The connatural metastability of the amorphous state in solution renders it very prone to transform into a crystalline state, inevitably leading to the formation of amorphous/crystalline heterostructures. (3) The understanding of the underlying relationships between amorphous/amorphous heterostructures and the MOR performance of electrocatalysts still remains scarce, primarily ascribed to the substantial difficulties in constructing such heterostructures and concerned theoretical simulations.[25,26] Thus, it is particularly desirable yet tricky to design and synthesize advanced electrocatalysts with abundant amorphous/amorphous heterostructures for optimizing the MOR kinetics, aiming to accomplish high-efficiency methanol electro-oxidation.

As a kind of positive electrode material for wide application in energy conversion and storage, transition-metal boride and borate have been demonstrated as attractive electrocatalysts with compelling catalytic activity and stability for small-molecule (H_2O, urea, methanol, and so forth) oxidation in a strongly alkaline medium.[27–29] Notably, both ultrathin nickel-based boride and borate nanosheets in an amorphous state have been achieved using a mature wet chemical strategy.[30–32] More preferably, amorphous metal boride is very susceptible to common oxidants and can be oxidized spontaneously into amorphous metal oxides and/or hydroxides once exposed to air or oxygen,[33] giving a giant opportunity to constitute an eligible amorphous/amorphous heterostructure for strengthening the MOR performance of non-noble metal electrocatalysts.

Inspired by the abovementioned discussions, herein, we construct an appealing amorphous/amorphous heterostructure consisting of amorphous nickel boride (denoted as a-Ni_xB) nanoparticles on amorphous nickel borate (denoted as a-Ni-B_i) ultrathin nanosheets through a rapid and simple room-temperature aqueous reaction under ambient conditions. Intriguingly, thanks to the synergistic effect between the ultrathin 2D configuration and amorphous/amorphous hetero-interfaces, the as-prepared amorphous Ni-B_i/Ni_xB (denoted as a-Ni-B_i/Ni_xB) hybrid catalyst is found to deliver promising electrocatalytic performance towards methanol oxidation, which affords a large anodic current density reaching up to 213 mA cm^{-2} at 0.6 V *vs.* Ag/AgCl, roughly 36.5 and 10.0 times higher than those of pure a-Ni_xB (5.84 mA cm^{-2}) and a-Ni-B_i (21.4 mA cm^{-2}), respectively. Meanwhile, taking the a-Ni-B_i/Ni_xB hybrid structures as a proof-of-concept example, we shed light on the substantial efficacy of amorphous/amorphous heterostructures in boosting the electrocatalytic MOR process. This work may present a new perspective for designing and synthesizing highly efficient electrocatalysts for future energy conversion applications.

Results and discussion

In this study, the fabrication of a-Ni-B_i/Ni_xB hybrid structures was easily accomplished by implementing a facile liquid-phase reaction at room temperature. As illustrated in Fig. 1(a), black precipitation appears instantly after adding BH_4^- to nickel ammonia ($Ni[NH_3]_6^{2+}$) aqueous solution. As demonstrated before, the strong reducibility of BH_4^- brings about the fast formation of the a-Ni_xB phase along with the reduction of Ni(II) to Ni(0). Simultaneously, the hydrolysis of BH_4^- gives rise to numerous borate anions that will immediately combine with nickel cations to generate an a-Ni-B_i phase, resulting in the establishment of a-Ni-B_i/Ni_xB heterostructures. It should be noted that the presence of a-Ni_xB can in turn catalyze the hydrolysis reaction of BH_4^- to stimulate *in situ* creation of more a-Ni-B_i surrounding the as-formed a-Ni_xB, endowing robust contact between the two components at the heterointerface.[34] In this composite, the a-Ni_xB component will gradually disappear with the assistance of bubbling oxygen during the aqueous reaction, eventually causing the formation of a bare a-Ni-B_i sample. First, powder X-ray diffraction (XRD) analysis was performed to characterize the phase composition of the resulting products. As observed from the XRD patterns in Fig. 1(b), a broad diffraction peak at around 45° in the case of a-Ni-B_i/Ni_xB discloses the amorphous nature of the a-Ni_xB component, while two evident diffraction peaks at 33.4° and 59.8° are readily assigned to the amorphous $Ni_3(BO_3)_2$ phase (JCPDS no. 26-1284), matching well with previously reported results.[35] This explicitly demonstrates the coexistence of a-Ni-B_i and a-Ni_xB phases in such hybrid structures. Of particular interest, the

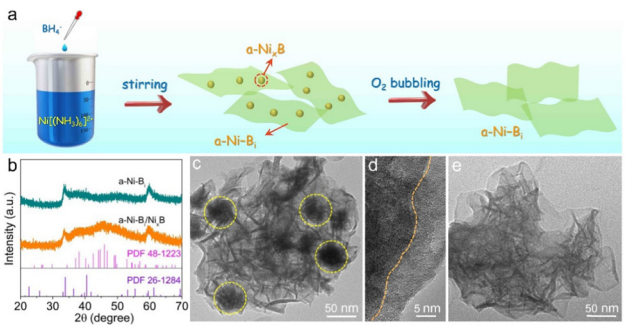

Fig. 1 (a) Schematic diagram for the fabrication of a-Ni-B_i/Ni_xB hybrid and a-Ni-Bi nanosheets. (b) XRD patterns of the as-prepared a-Ni-B_i/Ni_xB hybrid and a-Ni-Bi samples. (c) TEM and (d) HRTEM images of the a-Ni-B_i/Ni_xB hybrid sample. (e) TEM image of the ultrathin a-Ni-Bi nanosheets.

discernible disappearance of the as-mentioned broad diffraction peak in the XRD pattern of a-Ni-B_i reflects the consequent acquirement of the bare a-Ni-B_i sample upon oxygen treatment. Subsequently, transmission electron microscopy (TEM) was carried out to investigate the structural information of the samples. The TEM image in Fig. 1(c) indicates that the a-Ni-B_i component in the as-synthesized hybrid typically exhibits sheet-like morphology and its almost transparent feature signifies the ultrathin thickness of nanosheets. From the TEM image in Fig. S1 (ESI†), the thickness of the curled edge of nanosheets can be identified to be about 5.0 nm. As can be seen, the a-Ni_xB component, in the form of nanoparticles with an average size of ~50 nm (highlighted by yellow dashed circles), seems to be anchored evenly on the surface of a-Ni-B_i nanosheets, demonstrating their highly compatible structure with each other. Notably, the high-resolution TEM (HRTEM) image in Fig. 1(d) shows negligible crystal fringes in both a-Ni-B_i and a-Ni_xB sides, verifying the dominantly amorphous characteristics of the two components. Meanwhile, a close look visibly demonstrates the interface between the a-Ni_xB nanoparticle and the a-Ni-B_i nanosheet (marked by the orange dashed line), convincingly validating the successful construction of the a-Ni-B_i/Ni_xB heterostructures. As expected, no obvious particle-like morphology can be identified from the TEM image in Fig. 1(e), which strictly confirms the decomposition of the a-Ni_xB nanoparticles upon continuous oxygen bubbling, thereby leaving the pure a-Ni-B_i nanosheets.

X-ray photoelectron spectroscopy (XPS) was conducted to survey the surface composition and chemical state of the a-Ni-B_i nanosheets and the a-Ni-B_i/Ni_xB hybrid. As displayed in Fig. 2(a), the high-resolution Ni 2p XPS spectra in the case of a-Ni-B_i nanosheets exhibit two dominant Ni $2p_{3/2}$ and Ni $2p_{1/2}$ peaks at 855.7 and 873.2 eV, accompanied by two satellite peaks at 861.4 and 879.4 eV, typically indicative of the presence of bivalent nickel. While in the case of the a-Ni-B_i/Ni_xB hybrid, an additional peak at 852.3 eV can be well detected, which unambiguously authenticates the existence of metallic Ni^0 belonging to the Ni_xB nanoparticles.[36] As shown in Fig. 2(b), the B 1s spectra of a-Ni-B_i nanosheets can be clearly deconvoluted into two distinct peaks at 191.3 and 192.0 eV, both of which are assignable to the binding energy of B–O in boron oxide species. In addition to that, the peak located at 188.0 eV corresponds well to the signal of elemental boron in the case of the a-Ni-B_i/Ni_xB hybrid, further corroborating the existence of Ni_xB.[33] In the O1s spectrum (Fig. 2(c)), a pair of fitted peaks centered at 530.8 and 532.0 eV can be respectively attributed to the B–O–Ni bond in the a-Ni-B_i phase and the B–O bond in B_2O_3.[37,38] Concomitantly, the relative amount of the B–O–Ni species was briefly quantified in terms of the integral area of the corresponding peak, revealing that the relative content of the a-Ni-B_i phase in the a-Ni-B_i/Ni_xB hybrid increases distinctly with the operation of bubbling oxygen, which is in good accordance with the aforementioned results and discussion. In addition, N_2 adsorption–desorption tests were conducted to gain more surface structural information and insights into the pore structure of the obtained samples. According to the adsorption–desorption isotherm curves in Fig. 2(d), an obvious type-IV hysteresis loop can be recognized for both samples, representing the presence of plentiful mesopores correlative to appreciable slit-shaped pores, which probably originated from the sheet-like morphology of a-Ni-B_i. Evidently, Barrett–Joyner–Halenda (BJH) pore size distribution profiles (inset of Fig. 2(d)) display one prominent sharp peak corresponding to the pore diameters of about 3.39 and 3.66 nm respectively for a-Ni-B_i and a-Ni-B_i/Ni_xB samples (enlarged image in Fig. S2, ESI†), further proving the existence of abundant mesopores with a narrow range of size distribution. Also, this can be vividly confirmed by the TEM image in Fig. S3 (ESI†). Impressively, the a-Ni-B_i nanosheets show a much larger BJH pore volume of 0.936 $cm^3\ g^{-1}$ with respect to the a-Ni-B_i/Ni_xB hybrid sample (0.222 $cm^3\ g^{-1}$). Moreover, the Brunauer–Emmett–Teller (BET) surface area of the a-Ni-B_i sample is found to be 369.0 $m^2\ g^{-1}$, roughly 5.7 times higher than that of the a-Ni-B_i/Ni_xB hybrid sample (70.3 $cm^2\ g^{-1}$). These results suggest that the a-Ni-B_i component makes a significant contribution to the specific surface area of the a-Ni-B_i/Ni_xB hybrid sample due to its ultrathin 2D structure, which is favorable for the sufficient exposure of active sites for expediting the surface catalytic reaction.

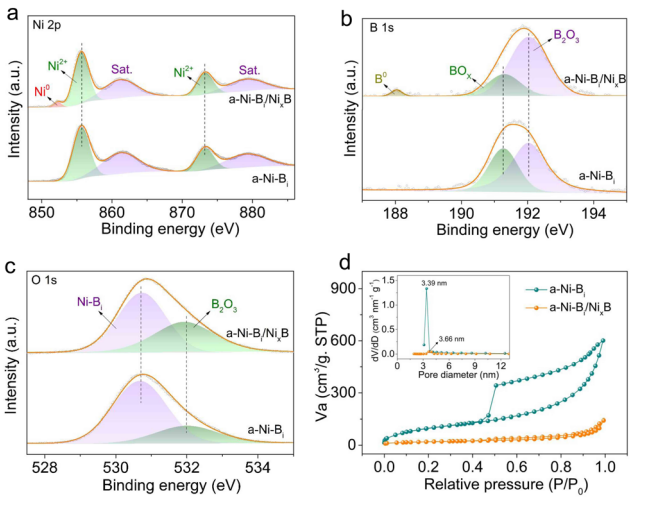

Fig. 2 High-resolution XPS spectra of (a) Ni 2p, (b) B 1s, and (c) O 1s, and (d) nitrogen adsorption–desorption isotherms and the corresponding pore size distribution curves (inset) of the a-Ni-B_i/Ni_xB hybrid and a-Ni-B_i samples.

In order to investigate the influence of amorphous/amorphous heterostructures on the electrochemical behaviors, a sequence of measurements was preliminarily carried out in a classic three-electrode system. In this study, a-Ni_xB nanoparticles were also synthesized as an essential reference using a similar liquid-phase reaction and the corresponding TEM image and XRD pattern are presented in Fig. S4 (ESI†). Prior to collecting data, all working electrodes need to be activated by consecutive cyclic voltammetry (CV) tests until the current signal reaches stabilization. Fig. 3(a) shows the CV curves of the a-Ni-B_i/Ni_xB hybrid sample recorded at different scan rates from 10 to 150 mV s^{-1} in 1 M KOH solution. As can be observed,

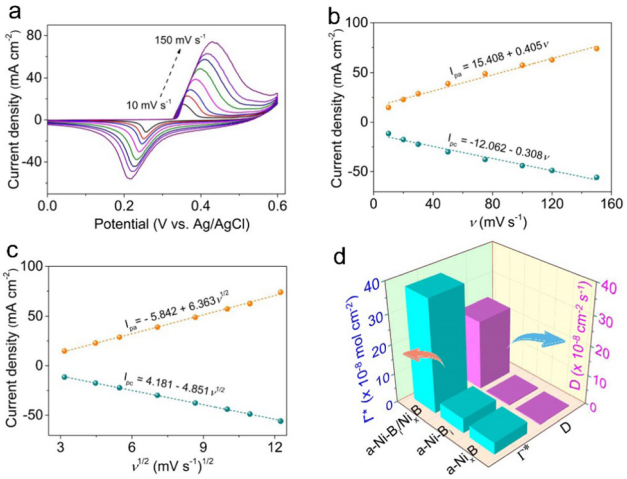

Fig. 3 (a) CV curves of the a-Ni-B_i/Ni$_x$B hybrid measured in 1 M KOH solution at different scan rates (10, 20, 50, 75, 100, 120 and 150 mV s^{-1}). The corresponding linear relationships between the anodic and cathodic current densities and (b) the scan rates, and (c) the square root of the scan rates. (d) The calculated Γ^* values and D values for the a-Ni-B_i/Ni$_x$B hybrid, a-Ni$_x$B and a-Ni-B_i samples.

the cathodic and anodic peaks located at around 0.35 V *vs.* Ag/AgCl are associated with the reversible Ni^{2+}/Ni^{3+} redox couple.[39] It is apparent that the a-Ni-B_i/Ni$_x$B hybrid shows a smaller potential gap (~100 mV) between the oxidation and reduction peak in the light of the CV curve at a scan rate of 10 mV s^{-1}, as compared to those of a-Ni$_x$B (~170 mV) and a-Ni-B_i (~180 mV) (Fig. S5, ESI†), which portends the more advantageous electrical conductivity and reversibility of the a-Ni-B_i/Ni$_x$B hybrid electrode.[40] Also, the redox peak intensity increases progressively with the increase of scan rate, exhibiting a good linear relationship between them (Fig. 3(b)). Furthermore, on the basis of the average of anodic and cathodic results, the surface coverage of the Ni^{2+}/Ni^{3+} redox species (Γ^*) for each electrode can be investigated. As summarized in Fig. 3(d), the Γ^* values for the a-Ni-B_i/Ni$_x$B hybrid, a-Ni$_x$B and a-Ni-B_i electrodes are respectively estimated to be 3.77×10^{-7}, 3.96×10^{-8} and 4.86×10^{-8} mol cm^{-2}, because of which the a-Ni-B_i/Ni$_x$B hybrid electrode shows a significantly greater oxidation peak current in comparison with the other two electrodes. This manifests the higher surface coverage of the Ni^{2+}/Ni^{3+} redox species on the a-Ni-B_i/Ni$_x$B hybrid catalyst during the electro-oxidation process. Moreover, both the anodic and cathodic peak current densities are linearly proportional to the square root of scan rates (Fig. 3(c)), revealing that the vigorous transformation between $Ni(OH)_2$ and NiOOH species in alkaline media is a diffusion-controlled process related to the solid-phase body of proton diffusion as reported before.[41] Consequently, the proton diffusion coefficient (D) is viewed as an imperative parameter for describing the electro-oxidation property of catalysts, which is evaluated by means of the Randles–Sevcik equation[42] together with the corresponding linear slopes in Fig. 3(c). As seen in Fig. 3(d), the a-Ni-B_i/Ni$_x$B hybrid electrode delivers the highest D value of 2.35×10^{-7} cm^2 s^{-1} among the three electrodes, nearly two orders of magnitude larger than those for the a-Ni$_x$B electrode (2.58×10^{-9} cm^2 s^{-1}) and the a-Ni-B_i electrode (3.82×10^{-9} cm^2 s^{-1}), which demonstrates the sharply promoted $Ni(OH)_2$/NiOOH redox process and thus the preferential generation of catalytically active NiOOH species at the amorphous/amorphous interface region, suggesting that the a-Ni-B_i/Ni$_x$B hybrid electrode can drive the MOR at a more negative onset potential.

With a view to shedding light on the efficacy of the amorphous/amorphous heterojunction structure on the electrocatalytic MOR performance, CV measurements were carried out in 1 M KOH electrolyte with and without 0.5 M methanol at a sweep rate of 50 mV s^{-1}. As shown in Fig. 4(a), the a-Ni-B_i/Ni$_x$B hybrid electrode exhibits a drastic boost in anodic current density after the addition of methanol, providing direct proof of its impactful electrochemical response towards methanol oxidation. By contrast, upon the addition of methanol, the slightly enhanced anodic current densities in the cases of the other two electrodes signify their mightily inferior electrocatalytic MOR performance (Fig. S6, ESI†). In terms of the CV curves obtained in 1 M KOH containing 0.5 M methanol (Fig. 4(b)), the hybrid catalyst of a-Ni-B_i/Ni$_x$B presents a lower onset potential (0.38 V *vs.* Ag/AgCl) and a greater anodic current density with respect to the a-Ni$_x$B and a-Ni-B_i catalysts, cogently demonstrating its superior electrocatalytic activity for the MOR. In particular, the a-Ni-B_i/Ni$_x$B hybrid electrode requires merely a low

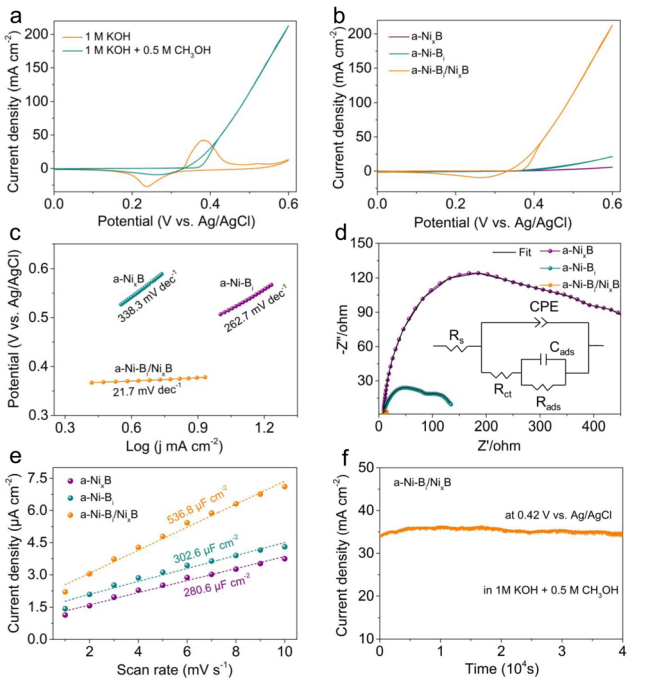

Fig. 4 (a) CV curves of the a-Ni-B_i/Ni$_x$B hybrid electrode obtained at a scan rate of 50 mV s^{-1} in 1 M KOH solution with and without 0.5 M methanol. (b) CV curves, (c) the corresponding Tafel plots, and (d) Nyquist plots of the a-Ni-B_i/Ni$_x$B hybrid, a-Ni$_x$B and a-Ni-B_i electrodes in 1 M KOH solution with 0.5 M methanol and the corresponding equivalent circuit for the fitted curves (inset). (e) Estimation of the C_{dl} values in 1 M KOH solution. (f) Chronoamperometric curve of the a-Ni-B_i/Ni$_x$B hybrid electrode recorded in 1 M KOH solution containing 0.5 M methanol.

potential of 387 mV *vs.* Ag/AgCl to drive a current density of 10 mA cm^{-2}, but that for the a-Ni-B_i electrode is found to be 506 mV *vs.* Ag/AgCl. Significantly, the a-Ni-B_i/Ni_xB electrode affords quite a large current density reaching up to 213 mA cm^{-2} at a potential of 0.6 V *vs.* Ag/AgCl, about 36.5 and 10.0 times higher than those of the a-Ni_xB and a-Ni-B_i electrodes, respectively. This value can be comparable to those of the most active MOR electrocatalysts reported recently under similar conditions (Table S1, ESI†). Meanwhile, as displayed in Fig. 4(c), the a-Ni-B_i/Ni_xB hybrid electrode possesses a Tafel slope of 21.7 mV dec^{-1}, markedly smaller than those of the a-Ni_xB electrode (338.3 mV dec^{-1}) and the a-Ni-B_i electrode (262.7 mV dec^{-1}), suggesting its more favorable electrocatalytic kinetics for the MOR. Furthermore, electrochemical impedance spectroscopy (EIS) was utilized to clarify the charge transfer kinetics during the electrocatalysis. As shown in Fig. 4(d), by virtue of the electrical equivalent circuit (inset), the Nyquist plots of the a-Ni-B_i/Ni_xB hybrid, a-Ni_xB and a-Ni-B_i electrodes can be fitted into two partially overlapped semicircles in high and low frequency regions. Obviously, among these tested electrodes, the a-Ni-B_i/Ni_xB hybrid electrode exhibits the smallest diameter of semicircle in the high frequency region, which demonstrates the lowest charge transfer resistance (R_{ct}) and significantly boosted MOR kinetics on the hybrid electrode since the semicircle at high frequency is closely associated with the R_{ct} during the electrochemical process.

As is known, the electrochemical active surface area (ECSA) and intrinsic reactivity of active sites have imperative influences on the overall electrocatalytic performance, which are deemed as two indispensable descriptors to evaluate high-efficiency MOR catalysts.[43,44] In this regard, the electric double-layer capacitance (C_{dl}) measurement was implemented to assess the ECSA of catalysts by collecting CV curves at different scan rates in a non-faradaic potential range (Fig. S7, ESI†). As shown in Fig. 4(e), the C_{dl} values for a-Ni_xB, a-Ni-B_i and a-Ni-B_i/Ni_xB hybrid electrodes are calculated to be 280.6, 302.6 and 536.8 μF cm^{-2}, respectively. This result can be indicative of the larger ECSA of the a-Ni-B_i/Ni_xB hybrid catalyst and thus reflects its more exposed active surface derived from the amorphous/amorphous heterojunction structures. As for the inherent activity of catalytic sites towards methanol oxidation, the CV curves for the MOR were normalized by their corresponding C_{dl} values. As can be seen from Fig. S8 (ESI†), the a-Ni-B_i/Ni_xB hybrid electrode attains a higher normalized MOR current density, which is respectively 19.1 and 5.6 folds larger than those of the a-Ni_xB and a-Ni-B_i electrodes at a potential of 0.6 V *vs.* Ag/AgCl, demonstrating its markedly increased intrinsic activity for the MOR. Additionally, as another vital parameter to appraise the catalytic performance, the long-term stability of the a-Ni-B_i/Ni_xB hybrid catalyst was further examined using a chronoamperometric curve at a potential of 0.42 V *vs.* Ag/AgCl. As shown in Fig. 4(f), no evident diminishment in current density can be observed even after 40 000 s of continuous operation in 1 M KOH containing 0.5 M methanol solution. Besides that, the TEM image after the stability test (Fig. S9, ESI†) exhibits negligible variations in the morphology of the a-Ni-B_i/Ni_xB hybrid catalyst, verifying its splendid electrocatalytic endurance as well as structural durability for the MOR under strong alkaline conditions, which makes it more beneficial for the potential application of DMFCs in future. Taken together, these results potently elucidate the exceptional contribution of the amorphous/amorphous heterostructures in promoting the electrocatalytic MOR process.

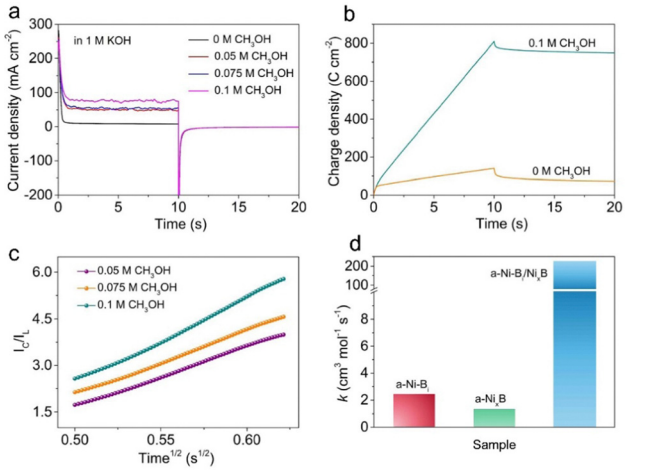

Fig. 5 (a) Double-potential-step chronoamperograms of the a-Ni-B_i/Ni_xB hybrid electrode performed in 1 M KOH solution at different methanol concentrations. (b) Dependence of the charge density (C cm^{-2}) on time and (c) the linear plots of the I_C/I_L ratio against (time)$^{1/2}$ achieved from the corresponding chronoamperograms in (a). (d) The calculated *k* values for the a-Ni-B_i/Ni_xB hybrid, a-Ni_xB and a-Ni-B_i electrodes.

To acquire more insights into the electrochemical process for the MOR, a suite of double-potential-step chronoamperometry tests were carried out by adopting the working potential at 0.6 V *vs.* Ag/AgCl (first step) and 0 V *vs.* Ag/AgCl (second step) in 1 M KOH with various methanol concentrations. As displayed in Fig. 5(a), the current density for the a-Ni-B_i/Ni_xB hybrid electrode becomes constant quickly and increases gradually as the methanol concentration increases at the forward potential step, embodying its rapid and stable electrochemical response for methanol oxidation. Obviously, the chronoamperogram of the a-Ni-B_i/Ni_xB hybrid electrode in the case of the absence of methanol exhibits an approximate symmetry between the forward and backward potential steps, which is correlated solely to the reversible electrochemical behavior of the $Ni(OH)_2$/NiOOH redox couple.[45] Nevertheless, in the case of the presence of methanol, the corresponding charge density obtained from the forward potential step is strikingly larger than that for the backward potential step, revealing that the methanol oxidation is an irreversible electrocatalytic process. Not only that, taking advantage of the collected chronoamperograms, the catalytic rate constant (*k*) for the electro-oxidation of methanol can be further determined in accordance with the following equation:[46]

$$I_C/I_L = \gamma^{1/2}[\pi^{1/2}\,\mathrm{erf}(\gamma^{1/2}) + \exp(-\gamma)/\gamma^{1/2}] \quad (1)$$

where I_C and I_L are the current densities of the tested electrodes in the presence and absence of methanol, respectively, $\gamma = kCt$ is

the argument of the error function, k represents the catalytic rate constant ($cm^3\ mol^{-1}\ s^{-1}$), C represents the methanol concentration (mol cm^{-3}) and t represents the elapsed time (s). Once $\gamma > 2$, the value of $erf(\gamma^{1/2})$ almost approaches 1 and the eqn (1) can be abbreviated to:

$$I_C/I_L = \pi^{1/2}\gamma^{1/2} = (\pi kCt)^{1/2} \quad (2)$$

According to eqn (2), good linear dependences are obtained by plotting the I_C/I_L ratio against $t^{1/2}$ (Fig. 5(c) and Fig. S10, ESI†). Therefore, the k value can be calculated from the slope of linear plots when the methanol concentration is given. As shown in Fig. 5(d), the average k value for the a-Ni-Bi/NixB hybrid electrode is found to be 2.25×10^6 $cm^3\ mol^{-1}\ s^{-1}$, about 180 and 92 times higher than those for the a-Ni_xB electrode (1.25×10^4 $cm^3\ mol^{-1}\ s^{-1}$) and the a-Ni-B_i electrode (2.44×10^4 $cm^3\ mol^{-1}\ s^{-1}$), respectively, emphasizing the noteworthy superiority of the amorphous/amorphous heterostructures in accelerating the electrocatalytic reaction rate of methanol oxidation.

Based on the experimental analysis and results, it can be inferred that the amorphous/amorphous heterointerface in conjunction with the ultrathin 2D structure is predominantly responsible for the significantly enhanced electrochemical MOR performance of the a-Ni-B_i/Ni_xB hybrid catalyst. On one hand, the combination of the advantages of a dominating amorphous structure and an ultrathin 2D configuration allows both the surface and inner atoms of the catalyst to be highly exposed to the electrolyte, which renders the increased electroactive surface area and mass transfer of reactants to speed up the MOR process. On the other hand, the amorphous/amorphous heterojunction structure empowers the catalyst with more exposure of catalytic sites and higher inherent reactivity, which enable the facilitation of charge transfer kinetics and thereby the ultimate optimization of the electrochemical MOR performance.

Conclusions

In summary, an a-Ni-B_i/Ni_xB composite with a dominating amorphous/amorphous heterojunction structure has been successfully synthesized using the liquid-phase reaction method at room temperature, which was subsequently used as a fascinating electrocatalyst for methanol oxidation. Meanwhile, taking the a-Ni-B_i/Ni_xB hybrid system as a satisfactory prototype, the efficacy of the amorphous/amorphous heterojunction structure in the noticeable promotion of the electrocatalytic MOR process is elaborately expounded. It was found that the amorphous/amorphous heterojunction structure is more conducive to the formation and exposure of active NiOOH species and thus achieving accelerated MOR kinetics. Benefiting from the synergistic interactions of the amorphous structure, heterointerface effect and ultrathin 2D configuration, the obtained a-Ni-B_i/Ni_xB hybrid catalyst exhibits impressive electrocatalytic MOR activity, with a smaller onset potential (0.38 V *vs.* Ag/AgCl), a lower Tafel slope (21.7 mV dec^{-1}) and a higher current density (213 mA cm^{-2} at 0.6 V *vs.* Ag/AgCl) relative to the a-Ni-B_i and a-Ni_xB catalysts, as well as remarkable long-term durability in an alkaline electrolyte. This work would offer a promising perspective for the design and construction of low-cost and high-efficiency electrocatalysts for DMFCs.

Experimental

Materials

All reagents were of analytical reagent grade and used as received without further purification.

Preparation of the a-Ni-B_i/Ni_xB hybrid catalyst

In a typical procedure, 1 mL of ammonia solution (28% wt) was added into 100 mL of 5 mM $NiCl_2$ aqueous solution to form a transparent mixture under constant stirring. After that, 1 mL of 1 M freshly prepared $NaBH_4$ aqueous solution (at about 5 °C maintained using an ice-bath) was added dropwise into the above solution with vigorous stirring and a black precipitate was formed instantaneously. After the termination of bubble generation, the resulting product was collected by centrifugation and washed with deionized water and ethanol several times. Then, it was dried at 60 °C overnight.

Preparation of the a-Ni-B_i catalyst

The synthesis of the a-Ni-B_i catalyst is similar to that of the a-Ni-B_i/Ni_xB hybrid catalyst, except that the freshly obtained black precipitate was treated with bubbling oxygen in the primordial mixture solution for another 60 minutes until the color of the mixture solution turned from black to light green.

Preparation of the a-Ni_xB catalyst

The a-Ni_xB catalyst was prepared through a liquid-phase reaction in conformity with previous literature.[47] Typically, 0.5 mmol $NiCl_2{\cdot}6H_2O$ was added into 15 mL of tetraethylene glycol (TEG) and deaerated under Ar gas. Thereafter, 15 mL of TEG solution containing 10 mmol $NaBH_4$ was injected into the above mixture solution and heated at 60 °C for 1 h under an Ar atmosphere. The product was centrifuged and washed with ethanol several times and then dried overnight at 60 °C.

Materials characterization

Powder X-ray diffraction (XRD) patterns were obtained using a Japan Rigaku D/max-rA system with Cu Kα radiation (λ = 1.542 Å). Transmission electron microscopy (TEM) and high-resolution transmission electron microscopy (HRTEM) were carried out on a JEOL-2100 TEM at an acceleration voltage of 200 kV. X-ray photoelectron spectroscopy (XPS) tests were taken on an ESCALAB MKII X-ray photoelectron spectrometer with an excitation source of Mg Kα = 1253.6 eV. Nitrogen adsorption–desorption tests were performed using a Micromeritics ASAP 2460 system.

Electrochemical measurements

Electrochemical tests were carried out on an electrochemical station (CHI660B) in a three-electrode system by adopting a graphite electrode as the counter electrode, a saturated Ag/AgCl electrode as the reference electrode and a glassy carbon electrode (GCE) with different catalysts as the working electrode. Typically, 4 mg of the as-prepared catalysts and 30 μL of Nafion solutions (5 wt%) were dispersed in 1 mL of isopropanol–water solution (volume ratio of 1 : 3) by vigorously sonicating for 1 h to obtain a homogeneous ink. Then, 5 μL of the resulting dispersion was evenly loaded onto a GCE (3 mm in diameter). Cyclic voltammetry (CV) was performed in 1 M KOH solution without and with 0.5 M methanol at a scan rate of 50 mV s^{-1}. Electrochemical impedance spectroscopy (EIS) measurements were carried out at a potential of 0.5 V *vs.* Ag/AgCl. The amplitude of the applied voltage was 5 mV, and the frequency range was 100 kHz to 1 Hz. The chronoamperometric test was implemented in 1 M KOH solution with 0.5 M methanol at a potential of 0.42 V *vs.* Ag/AgCl. The double layer capacitance (C_{dl}) of different catalysts was determined from the CV curves at different scan rates in a non-faradaic potential region (0.16–0.20 V *vs.* Ag/AgCl), which can be evaluated by plotting the $\Delta J = (J_a - J_c)$ at 0.18 V *vs.* Ag/AgCl against the scan rate. The C_{dl} value is half of the linear slope.

Conflicts of interest

There are no conflicts to declare.

Acknowledgements

This work was supported by the National Natural Science Foundation of China (21805149, 21675093), the Natural Science Foundation of Shandong Province of China (ZR2018BB012, 2015ZRB01A0D), and the Taishan Scholar Program of Shandong Province of China (ts20110829).

Notes and references

1 Q. B. Yuan, D. H. Duan, Y. H. Ma, G. Q. Wei, Z. L. Zhang, X. G. Hao and S. B. Liu, Performance of nano-nickel core wrapped with Pt crystalline thin film for methanol electrooxidation, *J. Power Sources*, 2014, **245**, 886–891.

2 N. Kakati, J. Maiti, S. H. Lee, S. H. Jee, B. Viswanathan and Y. S. Yoon, Anode Catalysts for Direct Methanol Fuel Cells in Acidic Media: Do We Have Any Alternative for Pt or Pt–Ru, *Chem. Rev.*, 2014, **114**, 12397–12429.

3 A. Badalyan and S. S. Stahl, Cooperative electrocatalytic alcohol oxidation with electron-proton-transfer mediators, *Nature*, 2016, **535**, 406–410.

4 Y. P. Wu, J. W. Tian, S. Liu, B. Li, J. Zhao, L. F. Ma, D. S. Li, Y. Q. Lan and X. H. Bu, A Highly Stable Bi-Microporous MOF with Cubane $[Ni_4(OH)_4]$ Cluster and Pore Space Partition for Electrocatalytic Methanol Oxidation Reaction, *Angew. Chem., Int. Ed.*, 2019, **58**, 12185–12189.

5 R. Ganesan and J. S. Lee, Tungsten Carbide Microspheres as a Noble-Metal-Economic Electrocatalyst for Methanol Oxidation, *Angew. Chem., Int. Ed.*, 2005, **44**, 6557–6560.

6 G. G. Liu, W. Zhou, Y. R. Ji, B. Chen, G. T. Fu, Q. B. Yun, S. M. Chen, Y. X. Lin, P. F. Yin, X. Y. Cui, J. W. Liu, F. Q. Meng, Q. H. Zhang, L. Song, L. Gu and H. Zhang, Hydrogen-Intercalation-Induced Lattice Expansion of Pd@Pt Core–Shell Nanoparticles for Highly Efficient Electrocatalytic Alcohol Oxidation, *J. Am. Chem. Soc.*, 2021, **143**, 11262–11270.

7 N. Yu, L. Kuai, Q. Wang and B. Y. Geng, Pt nanoparticles residing in the pores of porous $LaNiO_3$ nanocubes as high-efficiency electrocatalyst for direct methanol fuel cells, *Nanoscale*, 2012, **4**, 5386–5393.

8 H. Fang, J. H. Yang, M. Wen and Q. S. Wu, Nanoalloy Materials for Chemical Catalysis, *Adv. Mater.*, 2018, **30**, 1705698.

9 L. F. Xiong, B. Wang, H. R. Cai, H. J. Hao, J. Li, T. Yang and S. C. Yang, Understanding the doping effect on hydrogen evolution activity of transition-metal phosphides: Modeled with Ni_2P, *Appl. Catal., B*, 2021, **295**, 120283.

10 L. Zhao, M. Wen, Y. Tian, Q. Wu and Y. Fu, A novel structure of quasi-monolayered NiCo-bimetal-phosphide for superior electrochemical performance, *J. Energy Chem.*, 2022, **74**, 203–211.

11 Z. F. Wang, Y. K. Tian, M. Wen, Q. S. Wu, Q. J. Zhu and Y. Q. Fu, Integrating $CoNiSe_2$ Nanorod-arrays onto N-doped Sea-sponge-C spheres for highly efficient electrocatalysis of hydrogen evolution reaction, *Chem. Eng. J.*, 2022, **446**, 137335.

12 A. Baksi, S. H. Nandam, D. Wang, R. Kruk, M. R. Chellali, J. Ivanisenko, I. Gallino, H. Hahn and S. Bag, $Ni_{60}Nb_{40}$ Nanoglass for Tunable Magnetism and Methanol Oxidation, *ACS Appl. Nano Mater.*, 2020, **37**, 7252–7259.

13 A. A. Dubale, Y. Y. Zheng, H. L. Wang, R. Hübner, Y. Li, J. Yang, J. W. Zhang, N. K. Sethi, L. He, Z. K. Zheng and W. Liu, High-performance Bismuth-doped Nickel Aerogel Electrocatalyst for Methanol Oxidation Reaction, *Angew. Chem., Int. Ed.*, 2020, **59**, 13891–13899.

14 J. Cheng, X. J. Liu, J. F. Yang, J. Z. Liu, L. B. Zhang and L. X. Zhang, Three-dimensional Ni–MoN nanorod array as active and non-precious metal electrocatalyst for methanol oxidation reaction, *J. Electroanal. Chem.*, 2022, **906**, 116001.

15 Z. Y. Wang, L. Xu, F. Z. Huang, L. B. Qu, J. T. Li, K. A. Owusu, Z. Liu, Z. F. Lin, B. H. Xiang, X. Liu, K. N. Zhao, X. B. Liao, W. Yang, Y. B. Cheng and L. Q. Mai, Copper–Nickel Nitride Nanosheets as Efficient Bifunctional Catalysts for Hydrazine-Assisted Electrolytic Hydrogen Production, *Adv. Energy Mater.*, 2019, **9**, 1900390.

16 J. Yin, Q. H. Fan, Y. X. Li, F. Y. Cheng, P. P. Zhou, P. Xi and S. H. Sun, Ni–C–N Nanosheets as Catalyst for Hydrogen Evolution Reaction, *J. Am. Chem. Soc.*, 2016, **138**, 14546–14549.

17 X. Sun, H. T. Deng, W. G. Zhu, Z. Yu, C. Z. Wu and Y. Xie, Interface Engineering in Two-Dimensional Heterostructures: Towards an Advanced Catalyst for Ullmann Couplings, *Angew. Chem., Int. Ed.*, 2016, **55**, 1704–1709.

18 Q. F. Gong, L. Cheng, C. H. Liu, M. Zhang, Q. L. Feng, H. L. Ye, M. Zeng, L. M. Xie, Z. Liu and Y. G. Li, Ultrathin

$MoS_{2(1-x)}Se_{2x}$ Alloy Nanoflakes For Electrocatalytic Hydrogen Evolution Reaction, *ACS Catal.*, 2015, **5**, 2213–2219.

19 Y. K. Tian, A. J. Huang, Z. G. Wang, M. K. Wang, Q. S. Wu, Y. Shen, Q. J. Zhu, Y. Q. Fu and M. Wen, Two-dimensional hetero-nanostructured electrocatalyst of Ni/NiFe-layered double oxide for highly efficient hydrogen evolution reaction in alkaline medium, *Chem. Eng. J.*, 2021, **426**, 131827.

20 Y. R. Zheng, P. Wu, M. R. Gao, X. L. Zhang, F. Y. Gao, H. X. Ju, R. Wu, Q. Gao, R. You, W. X. Huang, S. J. Liu, S. W. Hu, J. F. Zhu, Z. Y. Li and S. H. Yu, Doping-induced structural phase transition in cobalt diselenide enables enhanced hydrogen evolution catalysis, *Nat. Commun.*, 2018, **9**, 2533.

21 N. L. Yang, H. F. Cheng, X. Z. Liu, Q. B. Yun, Y. Chen, B. Li, B. Chen, Z. C. Zhang, X. P. Chen, Q. P. Lu, J. T. Huang, Y. Zong, Y. H. Yang, L. Gu and H. Zhang, Amorphous/Crystalline Hetero-Phase Pd Nanosheets: One-Pot Synthesis and Highly Selective Hydrogenation Reaction, *Adv. Mater.*, 2018, **30**, 1803234.

22 Z. H. Dong, F. Lin, Y. H. Yao and L. F. Jiao, Crystalline $Ni(OH)_2$/Amorphous $NiMoO_x$ Mixed-Catalyst with Pt-Like Performance for Hydrogen Production, *Adv. Energy Mater.*, 2019, **9**, 1902703.

23 J. Hu, S. W. Li, Y. Z. Li, J. Wang, Y. C. Du, Z. H. Li, X. J. Han, J. M. Sun and P. Xu, A crystalline–amorphous Ni–$Ni(OH)_2$ core–shell catalyst for the alkaline hydrogen evolution reaction, *J. Mater. Chem. A*, 2020, **8**, 23323–23329.

24 L. Zhao, W. Zhou, M. Wen, Q. S. Wu, W. Y. Li, Y. Q. Fu, Q. J. Zhu, S. Chen and J. Q. Ran, Trifunctional Cu-Mesh/Cu_2O@FeO Nanoarrays for Highly Efficient Degradation of Antibiotic, Inactivation of Antibiotic-Resistant Bacteria, and Damage of Antibiotics Resistance Genes, *Energy Environ. Mater.*, 2023, **6**, e12299.

25 H. W. Zhao, F. S. Li, S. X. Wang and L. Guo, Wet Chemical Synthesis of Amorphous Nanomaterials with Well-Defined Morphologies, *Acc. Mater. Res.*, 2021, **2**, 804–815.

26 F. Z. Zhao, H. C. Liu, H. Y. Zhu, X. Y. Jiang, L. Q. Zhu, W. P. Li and H. N. Chen, Amorphous/amorphous Ni–P/$Ni(OH)_2$ heterostructure nanotubes for an efficient alkaline hydrogen evolution reaction, *J. Mater. Chem. A*, 2021, **9**, 10169–10179.

27 J. H. Li, H. Chen, Y. P. Liu, R. Q. Gao and X. X. Zou, *In situ* structural evolution of a nickel boride catalyst: synergistic geometric and electronic optimization for the oxygen evolution reaction, *J. Mater. Chem. A*, 2019, **7**, 5288–5294.

28 F. H. Wu, Z. L. Zhang, F. S. Zhang, D. H. Duan, Y. Li, G. Q. Wei, S. B. Liu, Q. B. Yuan, E. Z. Wang and X. G. Hao, Exploring the role of cobalt in promoting the electroactivity of amorphous Ni–B nanoparticles toward methanol oxidation, *Electrochim. Acta*, 2018, **287**, 115–123.

29 M. S. Amer, P. Arunachalam, A. M. Alsalman, A. M. Al-Mayouf, Z. A. Almutairi, S. A. Aladeemy and M. Hezam, Facile synthesis of amorphous nickel iron borate grown on carbon paper as stable electrode materials for promoted electrocatalytic urea oxidation, *Catal. Today*, 2022, **397**, 197–205.

30 T. He, J. M. V. Nsanzimana, R. J. Qi, J. Y. Zhang, M. Miao, Y. Yan, K. Qi, H. F. Liu and B. Y. Xia, Synthesis of amorphous boride nanosheets by the chemical reduction of Prussian blue analogs for efficient water electrolysis, *J. Mater. Chem. A*, 2018, **6**, 23289–23294.

31 M. Q. Yang, J. D. Dan, S. J. Pennycook, X. Lu, H. Zhu, Q. H. Xu, H. J. Fan and G. W. Ho, Ultrathin nickel boron oxide nanosheets assembled vertically on graphene: a new hybrid 2D material for enhanced photo/electro-catalysis, *Mater. Horiz.*, 2017, **45**, 885–894.

32 J. M. V. Nsanzimana, V. Reddu, Y. C. Peng, Z. F. Huang, C. Wang and X. Wang, Ultrathin Amorphous Iron–Nickel Boride Nanosheets for Highly Efficient Electrocatalytic Oxygen Production, *Chem. – Eur. J.*, 2018, **24**, 18502–18511.

33 J. Masa, I. Sinev, H. Mistry, E. Ventosa, M. De La Mata, J. Arbiol, M. Muhler, B. Roldan Cuenya and W. Schuhmann, Ultrathin High Surface Area Nickel Boride (Ni_xB) Nanosheets as Highly Efficient Electrocatalyst for Oxygen Evolution, *Adv. Energy Mater.*, 2017, **7**, 1700381.

34 W. J. Jiang, S. Niu, T. Tang, Q. H. Zhang, X. Z. Liu, Y. Zhang, Y. Y. Chen, J. H. Li, L. Gu, L. J. Wan and J. S. Hu, Reaction Pathway Studies, and Structural Characterization of Crystalline Ni_3B Nanoparticles, *Angew. Chem., Int. Ed.*, 2017, **56**, 6572–6577.

35 J. H. Ge, Y. C. Lai, M. H. Guan, Y. H. Xiao, J. Kuang and C. Z. Yang, Nickel borate with a 3D hierarchical structure as a robust and efficient electrocatalyst for urea oxidation, *Environ. Sci.: Nano*, 2021, **8**, 1326–1335.

36 F. L. Yang, P. Y. Han, N. Yao, G. Z. Cheng, S. L. Chen and W. Luo, Inter-regulated d-band centers of the Ni_3B/Ni heterostructure for boosting hydrogen electrooxidation in alkaline media, *Chem. Sci.*, 2020, **11**, 12118–12123.

37 C. Wu, Y. Bai, D. X. Liu, F. Wu, M. L. Pang and B. L. Yi, Ni–Co–B catalyst-promoted hydrogen generation by hydrolyzing $NaBH_4$ solution for *in situ* hydrogen supply of portable fuel cells, *Catal. Today*, 2011, **170**, 33–39.

38 R. Chen, H. Y. Wang, J. W. Miao, H. B. Yang and B. Liu, A flexible high-performance oxygen evolution electrode with three-dimensional $NiCo_2O_4$ core–shell nanowires, *Nano Energy*, 2015, **11**, 333–340.

39 H. L. Wang, H. S. Casalongue, Y. Y. Liang and H. J. Dai, $Ni(OH)_2$ Nanoplates Grown on Graphene as Advanced Electrochemical Pseudocapacitor Materials, *J. Am. Chem. Soc.*, 2010, **132**, 7472–7477.

40 Y. Z. Chen, T. F. Zhou, L. Li, W. K. Pang, X. M. He, Y. N. Liu and Z. P. Guo, Interfacial Engineering of Nickel Boride/Metaborate and Its Effect on High Energy Density Asymmetric Supercapacitors, *ACS Nano*, 2019, **13**, 9376–9385.

41 X. Cui, P. Xiao, J. Wang, M. Zhou, W. L. Guo, Y. Yang, Y. J. He, Z. W. Wang, Y. K. Yang, Y. H. Zhang and Z. Q. Lin, Highly Branched Metal Alloy Networks with Superior Activities for the Methanol Oxidation Reaction, *Angew. Chem., Int. Ed.*, 2017, **56**, 4488–4493.

42 A. A. Dubale, Y. Y. Zheng, H. L. Wang, R. Hübner, Y. Li, J. Yang, J. W. Zhang, N. K. Sethi, L. Q. He, Z. K. Zheng and W. Liu, High-performance Bismuth-doped Nickel Aerogel

Electrocatalyst for Methanol Oxidation Reaction, *Angew. Chem., Int. Ed.*, 2020, **59**, 13891–13899.

43 J. F. Xie, J. P. Xin, R. X. Wang, X. D. Zhang, F. C. Lei, H. C. Qu, P. Hao, G. W. Cui, B. Tang and Y. Xie, Sub-3 nm pores in two-dimensional nanomesh promoting the generation of electroactive phase for robust water oxidation, *Nano Energy*, 2018, **53**, 74–82.

44 W. L. Yang, X. P. Yang, C. M. Hou, B. J. Li, H. T. Gao, J. H. Lin and X. L. Luo, Rapid room-temperature fabrication of ultrathin $Ni(OH)_2$ nanoflakes with abundant edge sites for efficient urea oxidation, *Appl. Catal., B*, 2019, **259**, 11820–11825.

45 R. Ojani, J. B. Raoof, S. Fathi and S. Alami-Valikchali, Electrochemical behavior of Ni(II) incorporated in zeolite Y-modified carbon electrode: application for electrocatalytic oxidation of methanol in alkaline solution, *J. Solid State Electrochem.*, 2011, **15**, 1935–1941.

46 B. Kaur, R. Srivastava and B. Satpati, Highly Efficient CeO_2 Decorated Nano-ZSM-5 Catalyst for Electrochemical Oxidation of Methanol, *ACS Catal.*, 2016, **6**, 2654–2663.

47 Z. L. Schaefer, X. L. Ke, P. Schiffer and R. E. Schaak, Reaction Pathway Studies, and Structural Characterization of Crystalline Ni_3B Nanoparticles, *J. Phys. Chem. C*, 2008, **112**, 19846–19851.